SCIENCE CHINA
Technological Sciences

• Article •

January 2014 Vol.57 No.1: 101–116
doi: 10.1007/s11431-013-5423-y

Numerical simulation of unsteady cavitating flows around a transient pitching hydrofoil

HUANG Biao*, WU Qin & WANG GuoYu

School of Mechanical and Vehicular Engineering, Beijing Institute of Technology, Beijing 100081, China

Received September 6, 2013; accepted November 4, 2013; published online November 29, 2013

The objective of this paper is to improve the understanding of the influence of multiphase flow on the turbulent closure model, the interplay between vorticity fields and cavity dynamics around a pitching hydrofoil. The effects of pitching rate on the subcavitating and cavitating response of the pitching hydrofoil are also investigated. In particular, we focus on the interactions between cavity inception, growth, and shedding and the vortex flow structures, and their impacts on the hydrofoil performance. The calculations are 2-D and performed by solving the incompressible, multiphase Unsteady Reynolds Averaged Navier Stokes (URANS) equations via the commercial CFD code CFX. The k-ω SST (Shear Stress Transport) turbulence model is used along with the transport equation-based cavitation models. The density correction function is considered to reduce the eddy viscosity according to the computed local fluid mixture density. The calculation results are validated with experiments conducted by Ducoin et al. (see Computational and experimental investigation of flow over a transient pitching hydrofoil, Eur J Mech/B Fluids, 2009, 28: 728–743 and An experimental analysis of fluid structure interaction of a flexible hydrofoil in various flow regimes including cavitating flow, Eur J Mech B/fluids, 2012, 36: 63–74). Results are shown for a NACA66 hydrofoil subject to slow (quasi static, $\dot{\alpha} = 6°/\text{s}$, $\dot{\alpha}^* = 0.18$) and fast (dynamic, $\dot{\alpha} = 63°/\text{s}$, $\dot{\alpha}^* = 1.89$) pitching motions from α=0° to α=15°. Both subcavitaing (σ=8.0) and cavitating (σ=3.0) flows are considered. For subcavitating flow (σ=8.0), low frequency fluctuations have been observed when the leading edge vortex shedding occurs during stall, and delay of stall is observed with increasing pitching velocity. For cavitating flow (σ=3.0), small leading edge cavities are observed with the slow pitching case, which significantly modified the vortex dynamics at high angles of attack, leading to high frequency fluctuations of the hydrodynamic coefficients and different stall behaviors compared to the subcavitating flow at the same pitching rate. On the other hand, for the fast pitching case at σ=3.0, large-scale sheet/cloud cavitation is observed, the cavity behavior is unsteady and has a strong impact on the hydrodynamic response, which leads to high amplitude fluctuations of the hydrodynamic coefficients, as well as significant changes in the stall and post-stall behavior. The numerical results also show that the local density modification helps to reduce turbulent eddy viscosity in the cavitating region, which significantly modifies the cavity lengths and shedding frequencies, particularly for the fast pitching case. In general, compared with the experimental visualizations, the numerical results with local density correction have been found to agree well with experimental measurements and observations for both slow and fast transient pitching cases.

unsteady cavitating flow, pitching hydrofoil, turbulence model

Citation: Huang B, Wu Q, Wang G Y. Numerical simulation of unsteady cavitating flows around a transient pitching hydrofoil. Sci China Tech Sci, 2014, 57: 101–116, doi: 10.1007/s11431-013-5423-y

*Corresponding author (email: huangbiao@bit.edu.cn)

1 Introduction

The transient pitching hydrofoil problem is related to general performance of turbomachineries, rudders, hydrofoils, and general control surfaces, where a sudden change in the flow field is introduced by a rapid change in the effective angle of attack. In particular, when cavitation develops on the hydrofoils, unsteady shedding and breakdown occur violently, which leads to highly unsteady fluid forces on the hydrofoil, and hence may lead to strong transient hydrodynamic instabilities [1–3]. In such cases, it is important to understand the dynamic interactions and consequences of high amplitude load fluctuations with active/passive pitching/oscillating motion in both subcavitating and cavitating flows. The motivation is to improve the understanding of loads variations in unsteady conditions, such as off design condition, which can help the general design of marine structures to avoid structure failures, or to exploit the fluid structure interaction to improve performance and harvest energy [4].

Early studies of unsteady aerodynamics have been motivated mostly by the effects to avoid or reduce such undesirable effects as flutter, vibrations, and dynamic stall. A substantial number of experimental and numerical investigations on the flow structures and dynamic stall of the pitching and plunging airfoil have been conducted. McCroskey [5], Carr [6], Carr and McCroskey [7] and Ohmi [8] et al., experimentally examined the starting flow past a two-dimensional oscillating airfoil, and found that the reduced frequency was the dominant parameter of the flow. The experimental flow visualizations by Oshima and Natsume [9], Freymuth [10] and Koochesfahani [11] illustrate the formation and development of large vortical structures created by pitching and plunging airfoil. Lorber and Carta [12] performed experiments to study the aerodynamics of dynamic stall penetration at constant pitching rate and high Reynolds number. They demonstrated the influence of leading edge vorticity on the unsteady aerodynamic response during the stall regime. The vortex was strengthened by increasing the pitching rate and was weakened by increasing the Mach number. Lee and Gerontakos [13] conducted an experimental analysis of characteristics of the boundary layer and stall developing on an oscillating NACA 0012 airfoil at *Re*=135000. They found that for the static airfoil, the static-stalling mechanism was attributed to the bursting of a leading-edge laminar separation bubble, but for deep-stall oscillations, the leading-edge dynamic stall was found to originate with the sudden turbulent breakdown at a short distance downstream of the leading edge.

In addition to the dynamic response of pitching/plunging airfoil, the transient response of heaving/pitching hydrofoil has also been investigated. Triantafyllou et al. [14] conducted a series of tests to measure the forces and map the flow around a harmonically oscillating foil at zero average angle of attack, and special attention was paid to the parametric combination that results in the optimal formation of vortical patterns. Jumper et al. [15] performed wall pressure measurements on a rigid hydrofoil with different pitching velocities $\dot{\alpha}$ and upstream velocities V_∞. The results showed that the unsteady nature of the hydrodynamic loading was related to the non-dimensional similarity parameter $\dot{\alpha}^* = \dot{\alpha}c / V_\infty$, where c is the chord length. They reported that the relatively slow pitch rates had dramatic effects on both the delay of stall and the magnitude of the maximum lift coefficient. In addition, the dynamic stall was delayed with the increasing pitching velocity. Ducoin et al. [16] also conducted the joint computational and experimental investigation of flow over a transient NACA66 hydrofoil at *Re*=135000 for different pitching rates. They found that increasing the pitching velocity tended to delay the laminar-to-turbulence transition and even to suppress it for highest pitching velocity during the pitching up motion. During the pitching down motion, strong hysteresis was observed in hydrodynamic loading at the highest pitching rate.

It is well known that unsteady cavitation is an undesirable phenomenon because it usually implies negative design effects such as hydrodynamic losses, noise, vibration and efficiency reduction [17, 18], particularly when operating in spatially or temporally varying flow. Hence, it is necessary to understand the influence of unsteady cavitation on oscillating hydrofoil/blades. Recent work has explored the effects of unsteady cavitation on a stationary hydrofoil through experiment [19–23]. In the last few decades, the numerical simulation methods were developed to investigate the cavitating flow [24–32]. Cavitating flows are generally relatively high Reynolds number flows and hence the turbulence modeling plays an important role in the capture of prediction of the onset, growth, break-up and scale shedding of unsteady cavitating. In recent years, significant efforts have been made in the development of turbulence model for transient cavitating flows [26, 28, 33, 34].

There exist very limited experimental studies of cavitating flows around oscillating hydrofoils. Shen and Peterson [35, 36] conducted experimental studies to investigate the effect of pitching motion on the cavitation inception, growth, and collapse. They demonstrated that the development of the boundary layer of hydrofoil and cavitation inception was delayed with increasing oscillation frequency, the formation of cloud cavitation is suppressed at small reduced frequencies but intensified at higher reduced frequencies. Franc and Michel [37] investigated cavitating flow around an oscillating hydrofoil, experimentally. They found that in both steady and unsteady flow conditions, a cavity detached behind the laminar separation of the boundary and that transition to turbulence swept away an attached cavity. In addition, the primary effects of oscillation were convection and delay. Hart et al. [38] also conducted experimental studies

of unsteady cavitating flow around a 3D oscillating hydrofoil. They reported increasing hysteresis between cavitation inception and desinence with increasing the reduced frequency, and the effect was attributed to the changes in the hydrodynamic angle of attack of the leading edge moving relative to the freestream flow. Kato et al. [39] investigated the changes in dynamic loads and flow structure of a pitching hydrofoil with different pitching frequencies. They showed that the response was significantly different in the unlocked, quasi-locked, and locked-in range, where locked-in corresponds to the case when the cavity breakdown frequency is synchronized with the pitching frequency. Compared to experimental studies of cavitating flows around oscillating hydrofoils, even fewer numerical studies could be found in the open literature. Uchiyama [40] solved the isothermal mixture flow equations by approximating the fluid interfacial forces to simulate the bubbly flow around a pitching hydrofoil, but no experimental validations were presented.

Until now, there exist very limited numerical studies of cavitating flow around a pitching hydrofoil, which is a challenging problem because of uncertainty of the validity of turbulence models for transient flows, and needs to accommodate the transient body motion in turbulent, multiphase flows. The numerical simulations can help to complement experimental studies to provide a more comprehensive understanding of the complex physics involving a hydrofoil oscillating/ pitching in cavitating flow.

In this paper, the numerical models are firstly presented. The transport equation-based cavitation model and the *k-ω* SST (Shear Stress Transport) turbulence model are summarized, followed by description of a density correction model to take into account the local effects of compressibility in the cavitation. The foil geometry, fluid mesh, and boundary conditions are presented, followed by a brief summary of the experimental setup [41] used for validation of the computations. The results are then analyzed for a NACA 66 hydrofoil at two pitching rates (named the slow pitching velocity $\dot{\alpha} = 6^{\circ}/\mathrm{s},\ \dot{\alpha}^{*} = 0.18$ and the fast pitching velocity $\dot{\alpha} = 63^{\circ}/\mathrm{s},\ \dot{\alpha}^{*} = 1.89$) from α=0° to α=15°. To study the influence of turbulence models and their interaction with the unsteady cavity behavior, results are compared with and without the turbulent viscosity modifications. The variation of the predicted dynamic coefficients and flow structures for cavitating flows are compared with subcavitating flow for both slow pitching and fast pitching velocities, respectively.

2 Numerical models

2.1 Conservation of mass and momentum

The multiphase URANS equations, in their conservative form, for a Newtonian fluid without body forces and heat transfers, are presented below along with the mass transport equation in the Cartesian coordinates:

$$\frac{\partial \rho_{\mathrm{m}}}{\partial t} + \frac{\partial (\rho_{\mathrm{m}} u_j)}{\partial x_j} = 0, \tag{1}$$

$$\frac{\partial (\rho_{\mathrm{m}} u_i)}{\partial t} + \frac{\partial (\rho_m u_i u_j)}{\partial x_j} = -\frac{\partial p}{\partial x_i} + \frac{\partial}{\partial x_j}\left[(\mu_{\mathrm{m}} + \mu_{\Gamma})\left(\frac{\partial u_i}{\partial x_j} + \frac{\partial u_j}{\partial x_i} - \frac{2}{3}\frac{\partial u_k}{\partial x_k}\delta_{ij} \right) \right], \tag{2}$$

$$\frac{\partial \rho_{\mathrm{l}} \alpha_{\mathrm{l}}}{\partial t} + \frac{\partial (\rho_{\mathrm{l}} \alpha_{\mathrm{l}} u_j)}{\partial x_j} = \dot{m}^{+} + \dot{m}^{-}, \tag{3}$$

$$\rho_{\mathrm{m}} = \rho_{\mathrm{l}} \alpha_{\mathrm{l}} + \rho_{\mathrm{v}} \alpha_{\mathrm{v}}, \tag{4}$$

$$\mu_{\mathrm{m}} = \mu_{\mathrm{l}} \alpha_{\mathrm{l}} + \mu_{\mathrm{v}} \alpha_{\mathrm{v}}, \tag{5}$$

where, ρ_{m} is the mixture density, ρ_{l} is the liquid density, ρ_{v} is the vapor density, α_{v} is the vapor fraction, α_{l} is the liquid fraction, u is the velocity, p is the pressure, μ_{m} is the mixture laminar viscosity, μ_{l} and μ_{v} are respectively the liquid and vapor dynamic viscosities, and μ_{Γ} is the turbulent viscosity. The subscripts (i, j, k) denote the directions of the Cartesian coordinates. The source term $\dot{m}^{+}$, and the sink term $\dot{m}^{-}$, in eq. (3) represent the condensation and evaporation rates, respectively.

2.2 Merkle cavitation model

The cavitation model used in the present study is a popular phenomenological transport-based model proposed by Merkle et al. [42]. It was derived primarily based on dimensional arguments for large bubble clusters, and not for a single bubble. Both evaporation and condensation terms are assumed to be proportional to the difference between the local pressure and the vapor pressure. The mass fraction form of the evaporation and condensation terms can be written as

$$\dot{m}^{-} = \frac{C_{\mathrm{m\_dest}} \rho_{\mathrm{l}} \rho_{\mathrm{l}} \mathrm{MIN}(p - p_{\mathrm{v}}, 0)(1-\alpha_{\mathrm{v}})}{(0.50 \rho_{\mathrm{l}} U_{\infty}^{2}) \rho_{\mathrm{v}} t_{\infty}}, p < p_{\mathrm{v}}, \tag{6}$$

$$\dot{m}^{+} = \frac{C_{\mathrm{m\_prod}} \rho_{\mathrm{l}} \mathrm{MAX}(p - p_{\mathrm{v}}, 0) \alpha_{\mathrm{v}}}{(0.50 \rho_{\mathrm{l}} U_{\infty}^{2}) t_{\infty}}, p > p_{\mathrm{v}}. \tag{7}$$

In this work, the empirical factors are set to be $C_{\mathrm{m\_dest}}$ =1 and $C_{\mathrm{m\_prod}}$=80, the mean flow time scale is defined as $t_{\infty}=c/U_{\infty}$ [27], validation of Merkle model for the unsteady cavitating flows around a stationary and a pitching NACA66 hydrofoil have been presented in refs. [41, 43].

2.3 Turbulence model with local compressibility correction

In this work, the *k-ω* SST turbulence model [44] is applied.

The k-ω SST model switches to a k-ε behavior in the free-stream and therefore avoids the common k-ω problem that the model is too sensitive to the inlet free-stream turbulence properties. To account for the large density jump caused by cavitation, Coutier-Delgosha et al. [26] proposed to reduce the mixture turbulent viscosity based on the local vapor volume fraction α_v, hence, μ_{T_mod} in the following equation is used to replace μ_T in eq. (2):

$$f(n)=\frac{\rho_v+(1-\alpha_v)^n(\rho_l-\rho_v)}{\rho_v+(1-\alpha_v)(\rho_l-\rho_v)},\ \mu_{T\_mod}=\mu_T f(n). \quad (8)$$

The value of n depends on the desired physical resolution, Huang et al. [45] demonstrated that the choice of n values significantly affected the dynamic behavior of the unsteady cavitation around a stationary hydrofoil. The variation of the mixture density multiplied by $f(n)$ given in eq. (8) with the vapor volume fraction is shown in Figure 1 for n=1 (no modification) and n=3.

3 Experimental setup and description

Numerical predictions are compared with experimental measurements of a pitching NACA66 hydrofoil conducted at the cavitation tunnel at the Research Institute of French Naval Academy [16, 41]. The test section is 0.192 m^2 and 1 m long. The velocity ranges from 3 m s^{-1} to 15 m s^{-1}, and the pressure in the test section ranges from 30 mbar to 3 bars. The tunnel inflow turbulence intensity, defined as $V_{\infty\,rms}/V_\infty$ at the inlet of the test section, is about 2%. The chord length is c=0.15 m and the span length is s=0.191 m, and the angle of attack is defined as α. The transient pitching motion is defined as a single upward-downward motion from initial incidence of α=0° to the maximum incidence of α_{max}=15°, then back to α=0°. The rotation axis is located at the midchord, i.e. x/c=0.5 from the foil leading edge. The mean angular velocity is defined as $\dot{\alpha}=2\alpha_{max}/t_f$, where t_f is the final time of the transient pitching motion. In this paper, the slow angular velocity of 6°/s and fast angular velocity of 63°/s are both considered in subcavitating (σ=8.0) and cavitating (σ=3.0) flows. The nondimensional angular velocity based on the chord length c and the upstream velocity V_∞ is defined as $\dot{\alpha}^*=\dot{\alpha}\times c/V_\infty$. The variation of α with time for V_∞=5 m s^{-1} at the slow and fast pitching rates is given in Figures 2(a) and (b), respectively. The upward phase of the pitching cycle will be denoted with α^+ and the downward phase will be denoted with α^-.

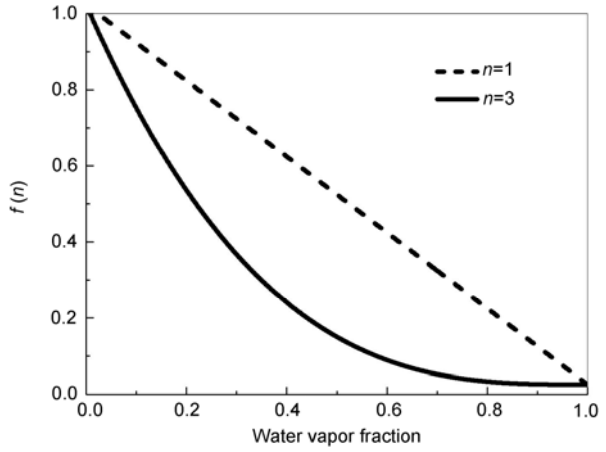

Figure 1 Variation of the mixture density correction with vapor volume fraction for n=1 and 3 used in eq. (8).

4 Numerical setup and description

The 2D fluid domain is shown in Figure 3(a), which corresponds to the height of the experimental test section at the French Naval Academy. The computational domain has an extent of about 5c upstream and 10c downstream of the foil to simulate near-infinite boundary conditions at the inlet and outlet. The 2D fluid mesh (shown in Figure 3(b)) is composed of 120000 elements with 50 structured elements across the foil boundary layer, which is selected to ensure $y^+=yu_\tau/\nu_m$ =1, where y is the thickness of the first cell from the foil surface, and u_τ is the wall frictional velocity. The regions outside the boundary layer have been discretized with unstructured triangular elements. Mesh refinements are performed at the foil leading edge, trailing edge, and in the wake region. A no-slip boundary condition is imposed on the hydrofoil surface, and symmetry conditions are imposed on the top and bottom boundaries of the tunnel. The outlet pressure is set to vary according to the cavitation number, defined as $\sigma=(p_\infty-p_v)/(0.5\rho_l V_\infty^2)$, where p_∞ is the tunnel pressure. The hydrofoil motion is taken into account using a

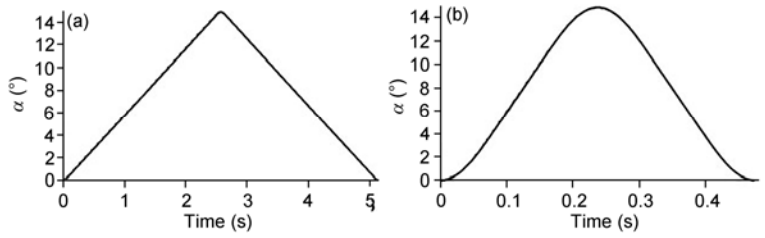

Figure 2 Variation of the measured geometric angle of attack α, with time for two pitching rates: (a) slow pitching $\dot{\alpha}=6°/s$, $\dot{\alpha}^*=0.18$; (b) fast pitching: $\dot{\alpha}=63°/s$, $\dot{\alpha}^*=1.89$.

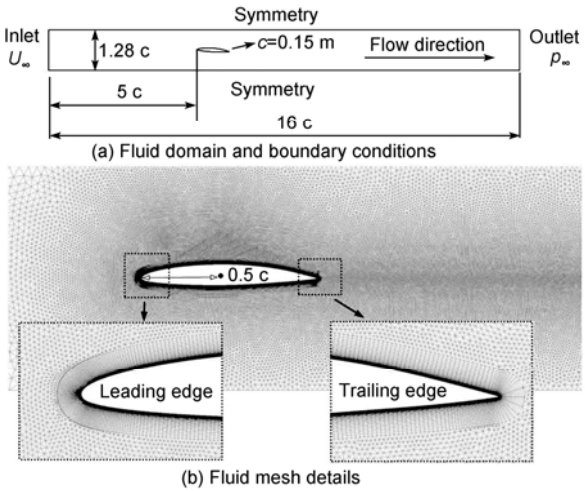

Figure 3 2D fluid mesh and boundary conditions.

changing boundary condition at the wall, the mesh is allowed to deform with the hydrofoil at each time step [16]. The time derivatives are calculated using a second-order backward Euler algorithm, and the spatial derivatives are calculated using a second-order upwind algorithm. The time step is chosen as $\Delta t=1\times10^{-4}$ for the computation, which gives an averaged CFL number of CFL= $V_\infty\Delta t/\Delta x=1$.

5 Results

5.1 Unsteady cavitating flow around a slowly pitching hydrofoil

Figure 4 shows the evolution of the lift ($Cl=L/(1/2\rho_l U_\infty^2 sc)$) coefficients with the geometric angle of attack for the slow pitching case ($\dot{\alpha}=6^\circ/\mathrm{s}$, $\dot{\alpha}^*=0.18$) in both subcavitating (σ=8.0) and cavitating (σ=3.0) conditions. The influence of the local mixture density correction on the turbulent eddy viscosity modification (eq. (8)) is investigated by applying n=1 and n=3. Also shown in Figure 4(a) are the measured lift coefficients for the same foil at static, subcavitating (σ=8.0) conditions, which compare well with the numerical predictions at the beginning of the upward rotation process. Figure 5 shows the evolution of vorticity contours at the five representative times (from t_1 to t_5) for the slow pitching case in subcavitating flow.

For subcavitating flow with σ=8.0, the hydrofoil response at the different phases of the flow cycle is explained below: from α^+=0° to α^+=4°, the lift coefficient increases almost linearly because the flow is quasi-steady and laminar, and then the change in slope or lift coefficient curve is observed in this phase of α^+=4° to α^+=6° coefficient which is due to the laminar to turbulent transition (laminar-to-turbulent transition occurs on the foil surface which affects the pressure distribution and changes the lift coefficient. More detail discussion of the laminar to turbulent transition can be found in ref. [16]. Between α^+=6° and α^+=13°, a clockwise ("–") trailing edge vortex (TEV) develops on the suction side of the foil surface (as shown in Figure 5(b), which corresponds to the time when the clockwise TEV is fully attached and stable), and grows (expands toward the leading edge) as α increases in the upward rotation process, which is responsible for the reduction in the slope of the lift coefficient curve. Small amplitude, high frequency fluctuations are observed in the lift, drag, and moment coefficients between α^+=11°–13° due to the fluctuations of the "–" clockwise TEV. Large amplitude, low frequency fluctuations of the hydrodynamic coefficients are observed because of leading edge (LE) stall at α^+=13° to α^-=12.5°. The detail developments of the LE vortex (LEV) are characterized by four phases, as shown in Figure 4(b) and 5: t_2 (formation of LEV on the suction side), t_3 (maximum extent of LEV while fully attached on the foil suction side), t_4 (partial shedding of LEV due to interaction with the "+" TEV) and t_5 (complete shedding of the vortex). It should be noted that the drop in load coefficients for subcavitating case in Figure 4 is due to the complete shedding of vortex at t_5. From α^-= 12.5° to α^-=0°, the light hysteresis effect could be observed due to a delay in reattachment, which is evident via the slight differences between the slopes at the corresponding angles in the upward and downward phases. Notice that

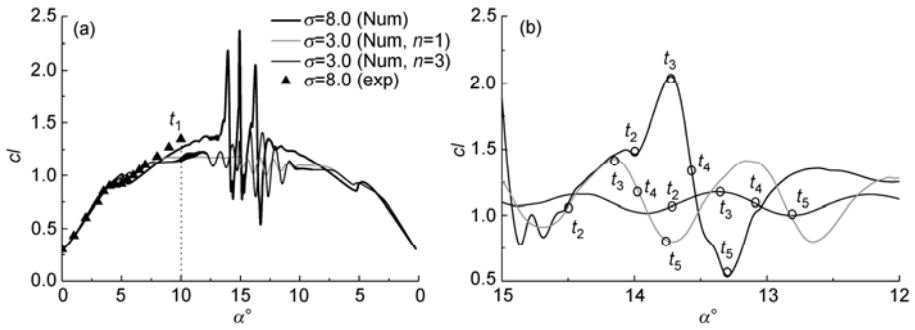

Figure 4 Comparisons of the predicted lift (*Cl*) for subcavitating (σ=8.0) and cavitating (σ=3.0) flows with n=1 and 3 for Re=750000, V_∞=5 m s^{-1}, $\dot{\alpha}=6^\circ/\mathrm{s}$, $\dot{\alpha}^*=0.18$. Also shown in (a) are the measured static lift coefficients at the fixed angle of attack. (a) Lift coefficient; (b) lift coefficient, zoomed (α^+= 15° to α^-=12°).

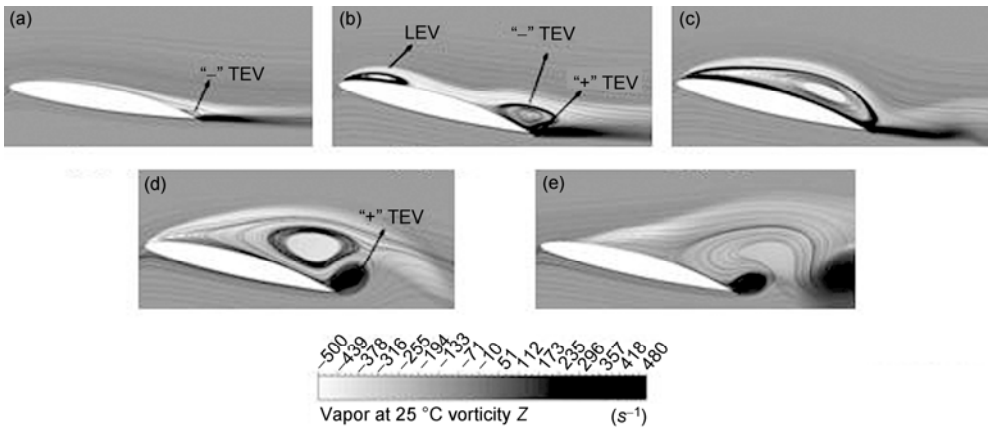

Figure 5 The predicted vorticity contours in the case of subcavitating for Re=750000, V_∞=5 m s^{-1}, $\dot{\alpha} = 6^\circ/\text{s}$, $\dot{\alpha}^* = 0.18$. (a) t_1: α^+=10 ; (b) t_2: α^-=14°; (c) t_3: α^-=13.75° ; (d) t_4: α^-=13.5°; (e) t_5: α^-=13.25°.

the flow transitions back to laminar at $\alpha^- \approx 5°$and the slopes of the hydrodynamic coefficients from α^-=5° to 0° are almost the same as from α^+=0° to 5°.

In order to better understand the influence of multiphase flow on the turbulent closure model, the interplay between vorticity fields and cavity dynamics around a pitching hydrofoil is studied. Compared with the lift coefficients obtained with n=1 and n=3 at σ=3.0 for the slow pitching case, the hydrofoil response at the different phases of the flow cycle in cavitating flow is explained below.

(i) α^+=0° to α^+=4°. The flow is subcavitation for both σ=3.0 and σ=8.0. Hence, the hydrodynamics responses in subcavitation and cavitation conditions, predicted with n=1 and n=3 are quite the same at the beginning of the upward rotation process.

(ii) α^+=4° to α^+=13°. Cavitation inception is observed at the leading edge as shown in Figures 6(a) and 7(a), which is responsible for the slight reduction in the slope of lift coefficient compared with the subcavitation. Small amplitude fluctuations could be observed due to the unsteady cavity fluctuations, especially for n=3.

(iii) α^+=13° to α^+=10°. Due to cavitation at the leading edge, at high angles of incidence, the hydrodynamic coefficients of cavitating flow experience much lower amplitude than for sub cavitating case, especially for n=1, which suggest that the flow vortex mechanism is changed due to cavity. It should be noted that fluctuation in load coefficients in cavitating case is due to stall, which is very different for the large amplitude of hydrodynamic coefficients due to the complete shedding of vortex in subcavitating flow.

(iv) α^-=10° to α^-=0°. Similar to the subcavitating case, the light hysteresis effect could be observed in the quasi-steady portion of the downward pitching phase.

Figures 6 and 7 show the predicted vapor fraction, turbulent kinetic energy and vorticity obtained with n=1 and n=3 for the slow pitching case in cavitating flow. It shows globally that the cavitation is relatively low and stays around the leading edge. The slope change and high frequency fluctuations observed on the hydrodynamic response between α^+=8° and α^+=12° in the cavitating cases, are due to the formation of a thin leading edge cavity on the suction side, which can be observed at the first rows of the pictures in Figures 6 and 7. For n=1 the lift coefficient is flat because the leading edge cavity is relatively stable, while it is seen to fluctuate for n=3 because the cavity structures become more unstable, inducing small partial shedding of vapor, which is due to the reduction in turbulent eddy viscosity when the density modification is applied. At higher angles of attack, the vorticity patterns appear to be significantly changed compared to subcavitating flow. For both n=1 and n=3 of cavitating cases, there is no significant leading edge vortex formed directly due to the presence of vapor at the leading edge which does not motivate a LEV generation. For n=1, the "–" clockwise TEV seems much more stable, as shown between the third and fourth rows of the pictures in Figure 6 and then fluctuates without detachment. For n=3, as the turbulent kinetic energy is seen to decrease together with higher vapor regions at the leading edge, this extends the vorticity at the leading edge, as shown at the second row of the pictures in Figure 7, and then eventually merges with "–" clockwise TEV . It is globally observed that the vorticity level is much higher than for n=1. The "–" clockwise vortex then covers the entire suction side of the hydrofoil and interacts with another unstable "+" counterclockwise TEV. As shown between the fourth and fifth rows of the pictures in Figure 7, the two vortices interact with each other and shed to create more significant fluctuations than n=1, which could be observed in hydrodynamic response (Figure 4). For cavitating flows, it should be noted that the vapor region at the leading edge can significantly change the flow structures and vorticity dynamic. From the above analysis, it can be concluded that the cavitation and the eddy viscosity modification change the vortex flow structures, which is shown to significantly modify the hydrofoil performance.

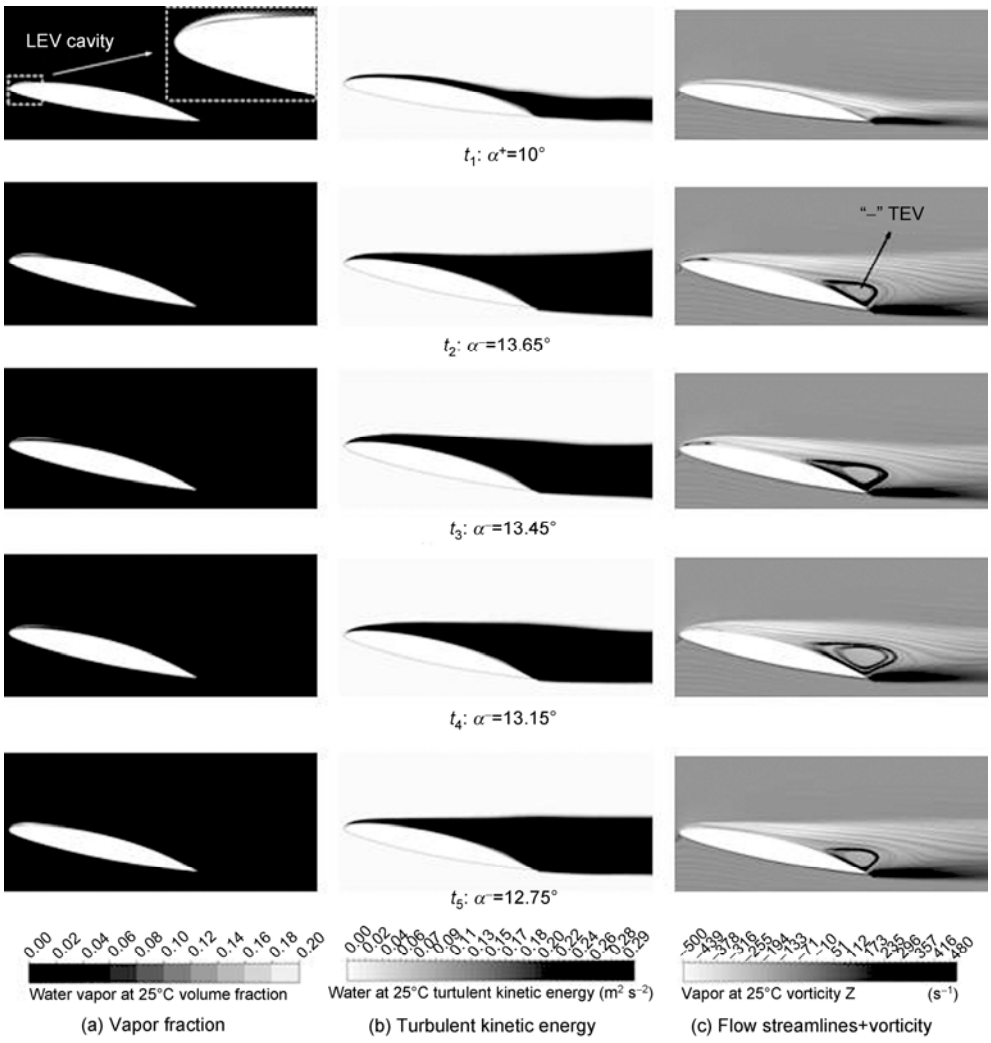

Figure 6 The predicted vapor fraction (a), turbulent kinetic energy (b), and vorticity (c) contours for α=3.0, Re=750000, V_∞= 5 m s^{-1}, $\dot{\alpha} = 6^\circ/\mathrm{s}$, $\dot{\alpha}^* = 0.18$, n=1.

Figure 8 shows the predicted pressure coefficients and evolution of the center of pressure at various angles of attack α for subcavitating (σ=8.0) and cavitating (σ=3.0) flows. The differences of vortex behavior between the subcavitating and cavitating can be related to the differences in adverse pressure gradient distributions at the leading edge. For subcavitating flow, the pressure gradient is so strong that it detaches the boundary layer at the leading edge to form an unstable vortex that shed. Whereas, for cavitating flow, the presence of vapor at the leading edge is seen to decrease the adverse pressure gradient, as shown by the constant pressure regions at t_1 in Figure 8, and hence it stabilizes the vorticity when the angle of attack increases.

For subcavitating flow, the low-pressure zone of the suction side is released by the growth of LEV, which significantly enhances the lift during pitching motion at t_3. With the vortex development, the center of pressure moves toward the midchord. It is observed that the pressure distribution at the trailing edge then fluctuates, which is due to the interaction and shedding of the vortex structures between t_4 and t_5, where the centre of pressure gradually moves toward the leading edge. For cavitating flows with n=1, the pressure coefficient seems much more stable, with small fluctuations at the trailing edge. With a turbulent viscosity modification (n=3), the pressure distribution is relatively unstable as compared to that for n=1 along with the interaction of the two contra-rotative vortices on the suction side.

Figure 9 shows the comparisons of the predicted vapor fraction contours predicted with the turbulent viscosity modification (n=3) with the observed cavitation patterns of ref. [41], although the experimental photographs show correspondence to a flexible hydrofoil, the deformations are small enough such that its impact could be negligible. Both the experimental visualizations and numerical results show that the slow pitching velocity is characterized by small cavities, as shown in Figure 9(a). The cavity length increases up to 0.2c at α^+=13° and has a relatively stable behavior. Small shedding of vapor structure is observed and tends to

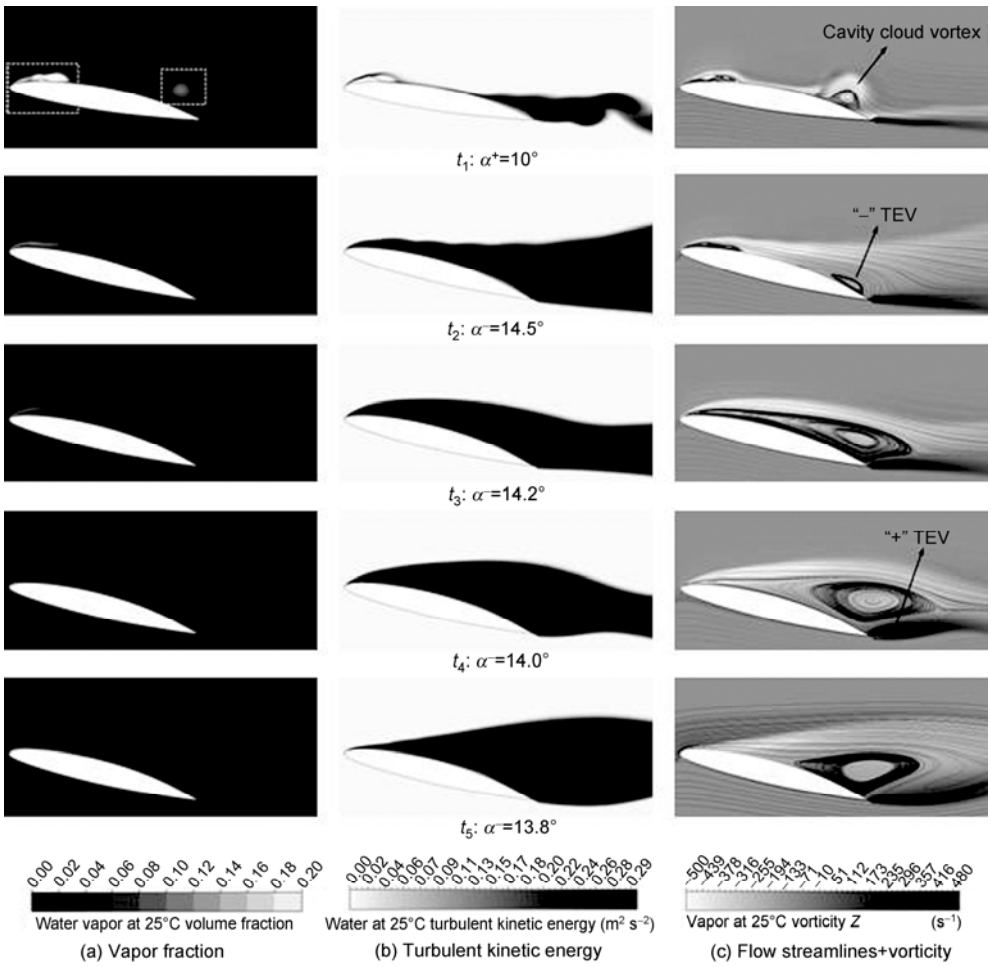

Figure 7 The predicted vapor fraction (a), turbulent kinetic energy (b), and vorticity (c) contours for σ=3.0, Re=750000, V_∞=5 m s^{-1}, $\dot{\alpha} = 6^\circ/\mathrm{s}$, $\dot{\alpha}^* = 0.18$, n=3.

develop when the cavity length increases. For α^+=14°, the cavitation induced by vortex shedding is observed.

5.2 Unsteady cavitating flow around a fast pitching hydrofoil

Figure 10 shows the evolution of the lift coefficients with the geometric angle of attack for the fast pitching case ($\dot{\alpha} = 63^\circ/\mathrm{s}$, $\dot{\alpha}^* = 1.89$) in both subcavitating (σ=8.0) and cavitating (σ=3.0) conditions. The influence of the local mixture density correction on the turbulent eddy viscosity modification (eq. (12)) is also investigated by applying n=1 and n=3. Figure 11 shows the evolution of kinetic energy and vorticity contours at the five representative times (from t_1 to t_5) for subcavitating flow with the fast pitching case in subcavitating flow.

For subcavitating flow with σ=8.0, the hydrofoil response at the different phases of the flow cycle is explained below: from α^+=0° to α^+=13°, the lift coefficients increase approximately linearly with the angle of attack. It should be noted that the change in slope observed near α^+=5° in the measured static lift coefficient is due to laminar to turbulent transition, which was captured using the same CFD model when the foil was pitched at the pitching rate of 6°/s in subcavitating conditions, as shown in Figure 4. At the pitching rate of 63°/s, the laminar to turbulent transition was suppressed and hence the sudden change in slope was not observed in the numerical predictions shown in Figure 10(a). LEV forms and develops between α^+=13° and α^-=14.5° gradually on the suction side of the foil section, as shown in Figures 11(a) and (b), which is responsible for the increase on the slope of the lift and drag coefficient curves. From α^-=14.5° to α^-=10°, the amplitudes of the lift, drag, and moment coefficients all undergo a sudden drop when LEV completely sheds. The details of the LE vortex (LEV) shedding for fast pitching are characterized by the four phases, as shown in Figures 10(b) and 11: t_2 (maximum extent of LEV while fully attached on the foil suction side), t_3 and t_4 (partial shedding of LEV due to the interaction with the "+" TEV) to t_5 (complete shedding of LEV). It has to be noted that only one shedding of vortex was observed due to the fast pitching motion, which is very different from the slow

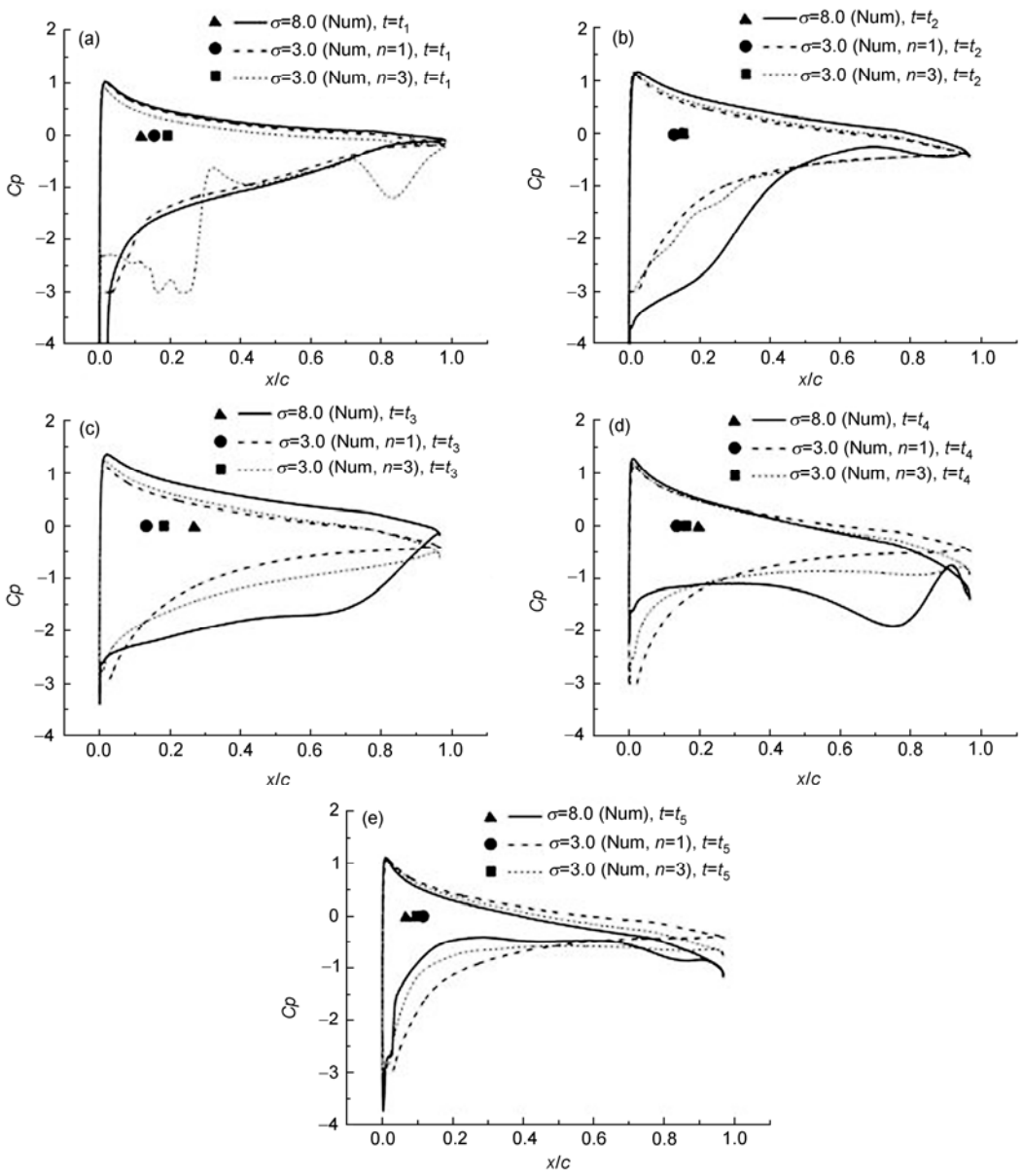

Figure 8 Comparisons of the predicted pressure coefficients and evolution of the centers of pressure at various geometric angles of attack α for subcavitating (σ=8.0) and cavitating (σ=3.0) flows for Re=750000, V_∞= 5 m s^{-1}, $\dot{\alpha} = 6^\circ/\mathrm{s}$, $\dot{\alpha}^* = 0.18$, n=1 and 3. (a) t_1; (b) t_2; (c) t_3; (d) t_4; (e) t_5.

pitching case.

From α^-= 10° to α^-=0°. Strong hysteresis is observed in response to the hydrodynamic loading, which is due to a delay in reattachment of the flow.

Compared with the lift coefficients predicted with n=1 and n=3, for the fast pitching case at σ=3.0, the hydrofoil response at the different phases of the flow cycle could be explained below:

(i) From α^+= 0° to α^+=8°. The flow is subcavitating for both n=1 and n=3. Hence, the predicted hydrodynamic coefficients are the same as the subcavitating case, no difference could be observed.

(ii) From α^+= 8° to α^+=14.5°. Cavitation inception is observed at the leading edge, and the extent of the sheet cavity increases with α. The lift and drag coefficients in the cavitating simulation with σ=3.0 are higher than those from the subcavitating simulation with σ=8.0. For σ=3.0, small amplitude, high frequency fluctuations could be observed due to cavity fluctuations, particularly near the cavity trailing edge, as can be seen evidently in the second and third rows of Figures 12 and 13. Higher frequency fluctuations are observed for n=3 because the cavity structure becomes more unstable due to the turbulent viscosity modifications.

(iii) From α^+=14.5° to α^-=13°. the amplitude of the lift, drag, and moment coefficients all undergo a sudden drop when the sheet cavity completely sheds and transforms to a

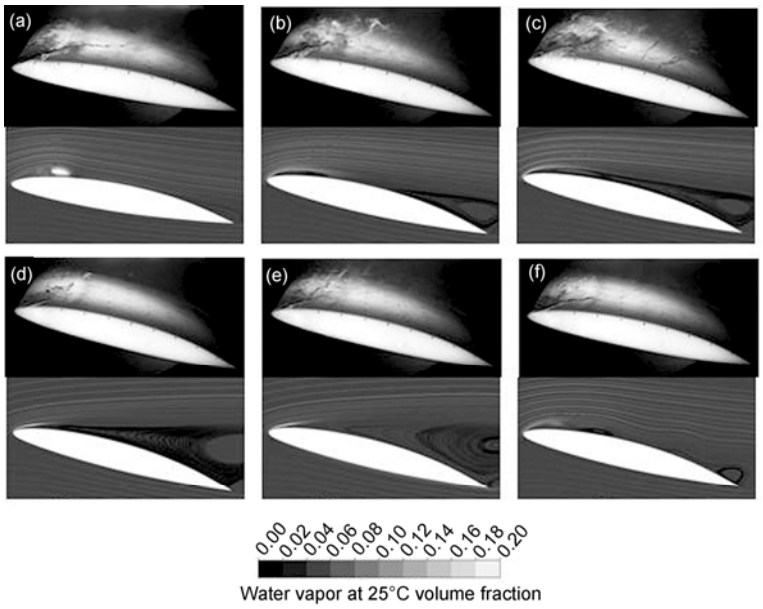

Figure 9 Comparisons of the predicted vapor fraction contours and flow streamlines (second rows of (a)–(f)) with experimental observations (first rows of (a)–(f))for σ=3.0, *Re*=750000, V_∞= 5 m s^{-1}, $\dot{\alpha} = 6^\circ/\mathrm{s}$, $\dot{\alpha}^* = 0.18$, n=3. (a) α^+=10°; (b) α^+=13°; (c) α^+=14°; (d) α^+=15°; (e) α^-=14°; (f) α^-=12.5°;

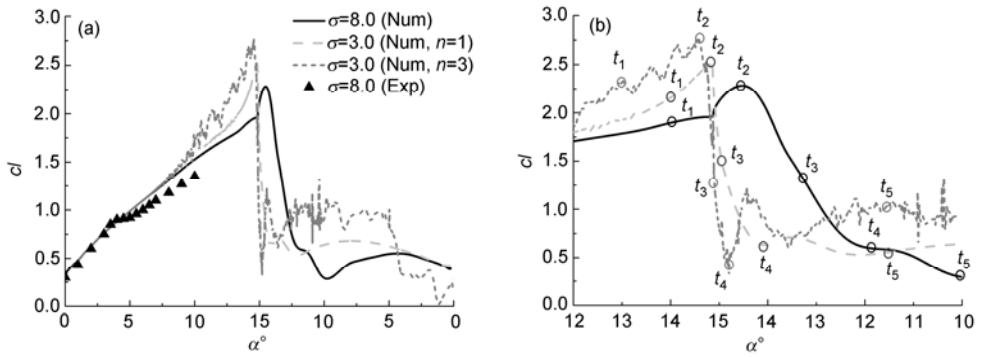

Figure 10 Comparison of the predicted lift (*Cl*) coefficients for subcavitating (σ=8.0) and cavitating (σ=3.0) flows with n=1 and 3 for *Re*=750000, V_∞=5 m s^{-1}, $\dot{\alpha} = 63^\circ/\mathrm{s}$, $\dot{\alpha}^* = 1.89$. Also shown in (a) are the measured static lift coefficients at the fixed angle of attack..(a) Lift coefficient; (b) lift coefficient, zoomed (α^+= 12° to α^-=10°).

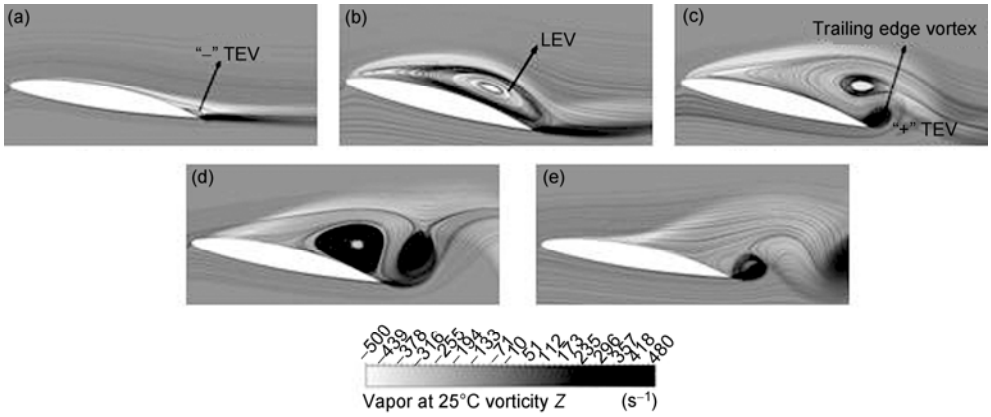

Figure 11 The predicted vorticity contours, in the case of subcavitating for σ=8.0, *Re*=750000, V_∞=5 m s^{-1}, $\dot{\alpha} = 63^\circ/\mathrm{s}$, $\dot{\alpha}^* = 1.89$. (a) t_1: α^+=14°; (b) t_2: α^+=14.5°; (c) t_3: α^-=13.4°; (d) t_4: α^-=11.85°; (e) t_5: α^-=10°;

cloud cavity downstream, as shown between the third and fourth rows of the pictures in Figures 12 and 13. It should be noted that the drop in the load coefficients for the sub-cavitating case is due to stall, which is very different, from the drop due to complete shedding of the sheet cavity, and occurs later.

(iv) From α^-=13° to α^-=0°. Strong hysteresis could also be observed in cavitating hydrodynamic load coefficients. In the cavitating case with σ=3.0, the load coefficients are not only affected by the delay in reattachment of the flow, but also by the rebound and subsequent collapse of the secondary sheet/cloud cavitation, especially for n=3.

Figures 12 and 13 present the predicted vapor fraction, turbulent kinetic energy and vorticity obtained with n=1 and n=3 for the fast pitching hydrofoil. It is observed that the fast pitching velocity is characterized by sheet/cloud cavitation. Due to the sheet cavitation at the leading edge, the slope change and relatively high frequency fluctuations are observed on the hydrodynamic response between α^+= 8° and α^+=14.5° for the cavitating results, which can be observed at the first row of the pictures in Figures 12 and 13, the hydrodynamic response is seen to fluctuate more significantly for n=3 because the cavity is more unstable than for n=1. For n=1, as shown in Figure 12, the over prediction of turbulent viscosity without the density correction reduces the interaction between the vorticity and the cavitation, the flow is characterized by a leading edge vortex that develops through the suction side between the first and second rows of the pictures in Figure 12, interacts with a trailing edge vortex between the third and fourth rows and shed in the wake at the fifth row. The over-predicted turbulent viscosity near the wall reduces the vorticity magnitude, and the vortex generates clouds at the trailing edge of the hydrofoil, then the clouds convect in the wake between the third and forth rows of the pictures in Figure 12. For n=3, the level of turbulent kinetic energy in the cavity seems much lower, resulting in a high vorticity near the wall and much higher level of vapor in the unsteady sheet cavity that grows up to the trailing edge between the first and second rows of the pictures in Figure 13. Moreover, a re-entrant jet is observed that allows the cavity to shed between the third and forth rows, a large cloud is generated in the trailing edge vortex. During the downward motion, after the shedding of the primary sheet cavity, small-scale cavity structures were

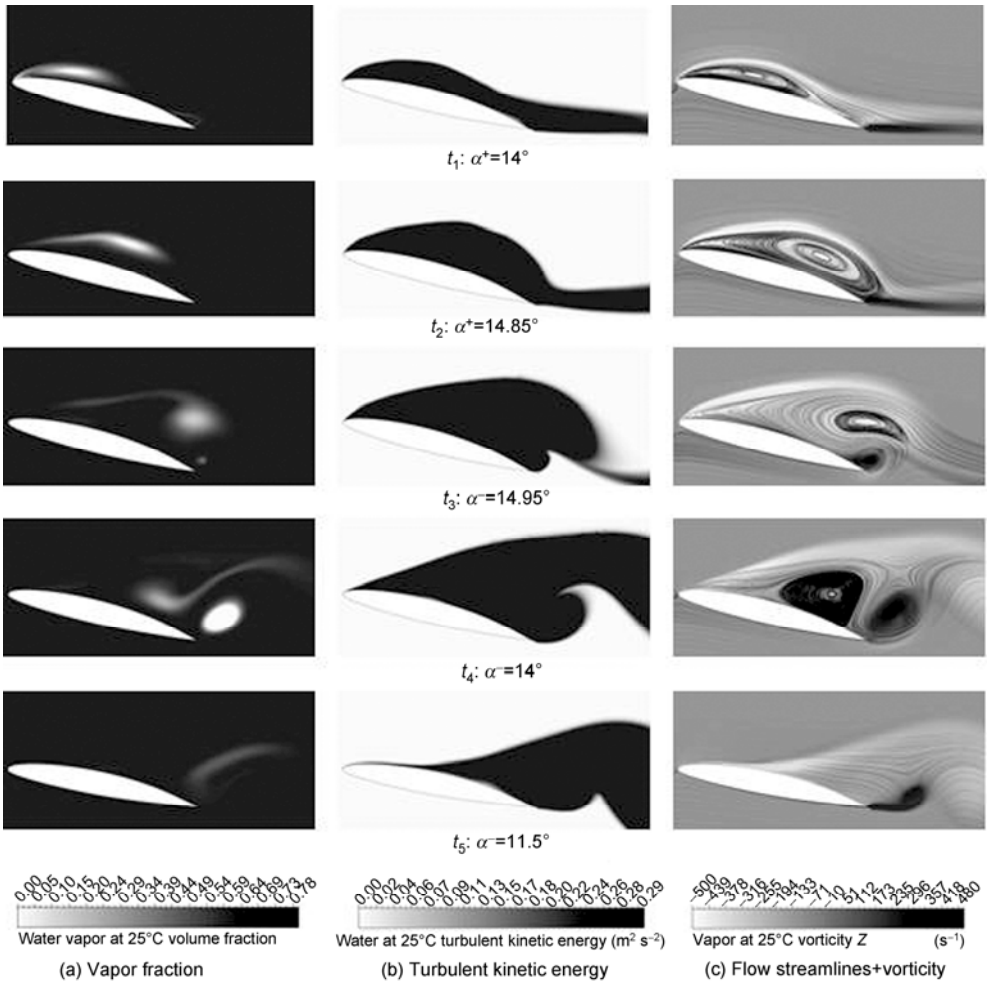

Figure 12 The predicted vapor fraction (a), turbulent kinetic energy (b), and vorticity (c) contours for σ=3.0, Re=750000, V_∞= 5 m s^{-1}, $\dot{\alpha} = 63^\circ/\mathrm{s}$, $\dot{\alpha}^* = 1.89$, n=1.

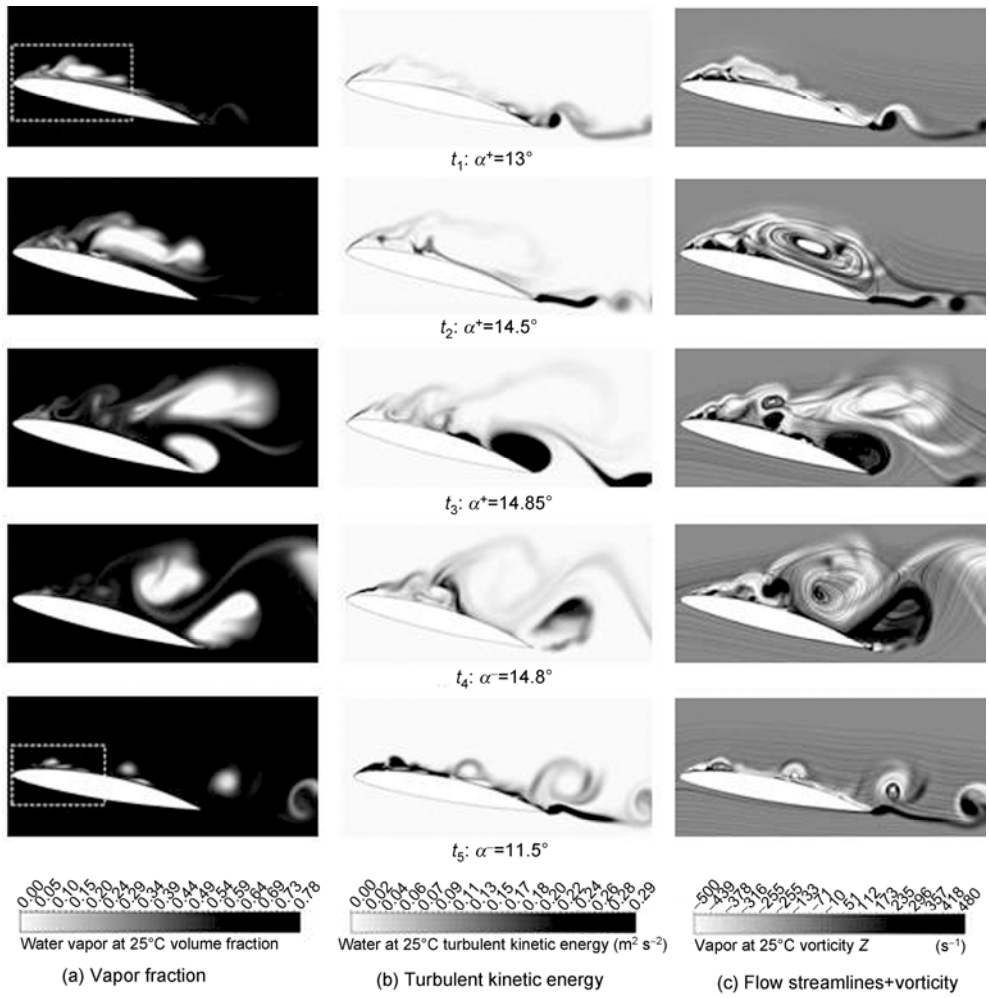

Figure 13 The predicted vapor fraction (a), turbulent kinetic energy (b), and vorticity (c) contours for σ=3.0, Re=750000, V_∞= 5 m s^{-1}, $\dot{\alpha} = 63^\circ/\mathrm{s}$, $\dot{\alpha}^* = 1.89$, n=3.

predicted. The effect of turbulent viscosity modification is responsible for the different time-history of the load coefficients between σ=8.0 and σ=3.0 with n=1 and n=3, as shown in Figure 10. From the above analysis, it can be concluded that for subcavitating flow, the separation of the leading edge vortex over the suction side is accompanied by a sudden loss of lift and a decrease in moment coefficient, but for cavitating flow, the predicted cavity has an unstable behavior, especially for n=3, the detachment and collapse of cavity play a primary role in the sudden decline of the lift.

Figure 14 shows the predicted pressure coefficient and evolution of the center of pressure at various angles of attack α for subcavitating (σ=8.0) and cavitating (σ=3.0) flows. For subcavitating flow, the adverse pressure gradients at the leading edge are relatively high and LEV forms and develops along the suction of the hydrofoil. The development of LEV globally decreases the pressure, which enhances the lift coefficient and the center of pressure moves towards the midchord. From t_3 to t_5, the pressure distributions fluctuate at the trailing edge with the interaction between the leading edge and the trailing edge vortex, and the center of pressure moves toward the leading edge accompanied by the vortex shedding.

For cavitating flows with n=1, the pressure distribution in the leading edge sheet cavity is flat and smooth due to the influence of vortex structures at the leading edge at t_1. From t_2 to t_5, the development and shedding of vortex structure significantly influence the distribution of the pressure, which is close to the subcavitating case. For n=3, the evolution of pressure distributions is largely dependent on the unstable cavity behavior, including the development, detachment and collapse of the sheet/cloud cavity. This results in significant fluctuations of the center of pressure and high variation of lift coefficients, as shown in Figure 10.

Figure 15 shows the comparisons of the predicted vapor fraction contours with turbulent viscosity modification (n=3) with the observed cavitation patterns of ref. [41] for the fast pitching case. Both the numerical and experimental results show that a relatively long sheet cavity which develops from the leading edge up to 0.6c is observed at α^+=14°.

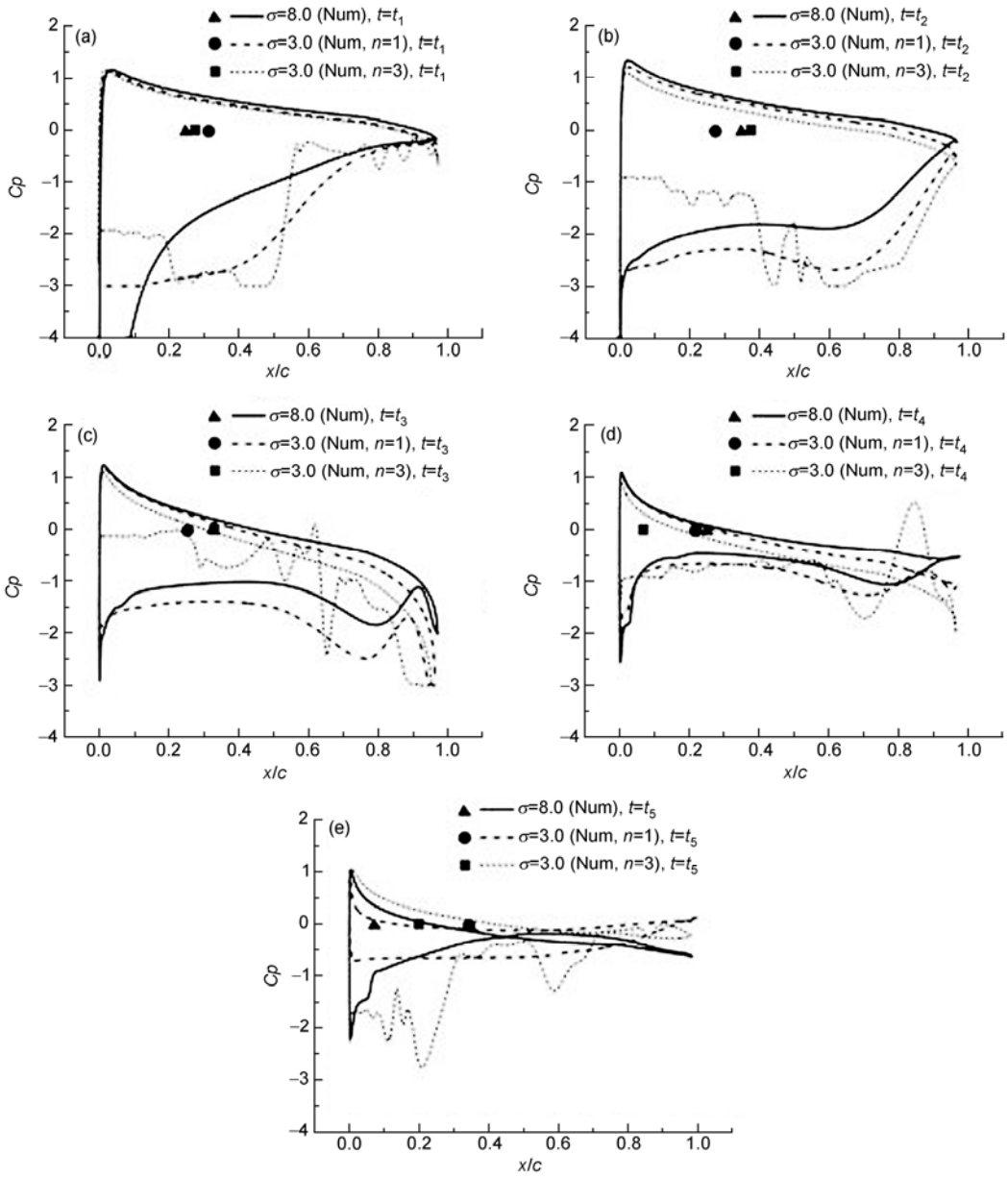

Figure 14 Comparisons of the predicted pressure coefficients and evolution of the centers of pressure at various geometric angles of attack for subcavitating (σ=8.0) and cavitating (σ=3.0) flows for Re=750000, V_∞= 5 m s^{-1}, $\dot{\alpha} = 63^\circ$/s, $\dot{\alpha}^* = 1.89$, n=1 and 3. (a) t_1; (b) t_2; (c) t_3; (d) t_4; (e) t_5.

Then, the sheet cavity breaks down into a large vapor-filled structure and generates a large pounding sound, Figure 16 highlights the significance of the re-entrant jet to show the representative unsteady behaviors between α^+=14.5° and α^+=14.7°, the re-entrant jet interacts with the cavity as it moves upstream. As the re-entrant flow reaches the vicinity of cavity leading edge, the sheet cavity is lifted away from the hydrofoil surface and sheds downstream in the form of a cloud cavity. The numerical results are the same as the analysis of the mechanics of typical cloud sheddings [45, 46]. This vapor filled structure is convected in the wake leading edge vortex pattern at α^-=14°. During the return step to α^-=0°, such as α^-=11.5°, the attached cavities appear at the leading edge again and disappear quickly together with the decrease of angle of incidence. Overall, the numerical results perform better compared with the experimental visualizations.

6 Conclusions

The predictive capabilities is investigated for the prediction of cavitation flow around a pitching NACA66 hydrofoil at two frequencies (named the slow pitching velocity $\dot{\alpha} = 6^\circ$/s $\dot{\alpha}^* = 0.18$ and the fast pitching velocity $\dot{\alpha} = 63^\circ$/s $\dot{\alpha}^* = 1.89$) at Re=750000 for subcavitaing (σ=8.0) and

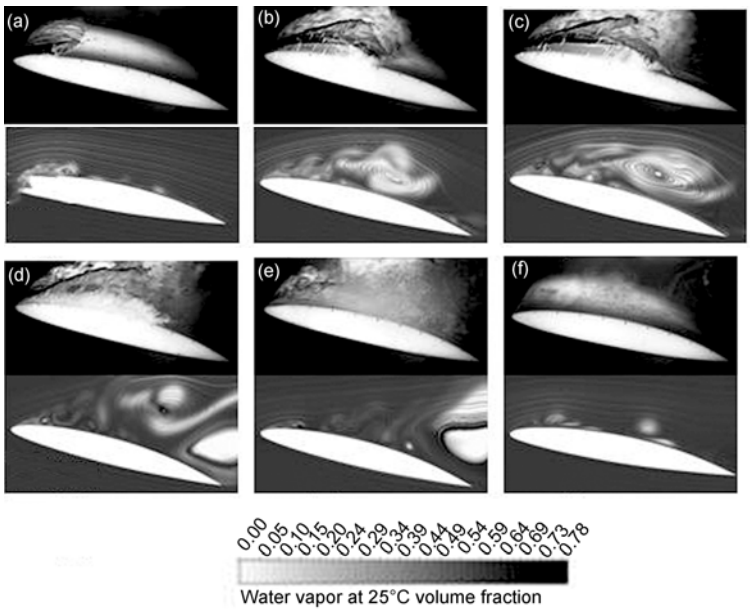

Figure 15 Comparisons of the predicted vapor fraction contours and flow streamlines (second rows of (a)–(f)) with experimental observations (first rows of (a)–(f)) for σ=3.0, Re=750000, V_∞=5 m s^{-1}, $\dot{\alpha} = 63^\circ/\text{s}$, $\dot{\alpha}^* = 1.89$, n=3. (a) α^+=12°; (b) α^+=14°; (c) α^+=14.5°; (d) α^+=15°; (e) α^-=14°; (f) α^-=11.5°.

cavitating (σ=3.0) conditions. In addition to the application of different levels of density correction to the turbulent viscosity and the possible effects of compressibility on the cavitation dynamics, the effects on pitching rates on the subcavitating and cavitation dynamics are also considered to investigate the interaction between cavitation and turbulent flows. Comparisons on the hydrodynamic coefficient flow structures predicted for both subcavitating and cavitating are shown. The general conclusions of the paper are drawn below.

1) For subcavitating flow (σ=8.0), the hydrodynamic coefficients are affected by the laminar to turbulent transition at low angles of attack in the case of a slow pitching velocity whereas the high pitching velocity suppresses this effect. At high angles of attack, high fluctuations of the hydrodynamics coefficients with low frequency are observed. This is due to the formation and development of leading edge vortex. For the fast pitching velocity, the hydrofoil response strongly significantly leads to high lift values at stall together with a strong hysteresis effect during the downward motion.

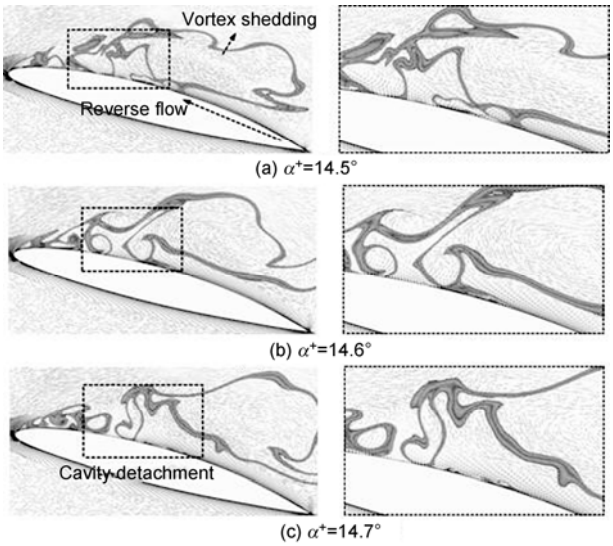

Figure 16 The predicted development of re-entrant jet and detached cavity for σ=3.0, Re=750000, V_∞= 5 m s^{-1}, $\dot{\alpha} = 63^\circ/\text{s}$, $\dot{\alpha}^* = 1.89$, n=3.

2) Cavitation behavior is observed (σ=3.0). For the slow pitching velocity, small leading edge cavities are observed, and then leading edge vortex shedding occurs with residual cavitation. The presence of cavity at the leading edge reduces the adverse pressure gradient, which modifies significantly the vortex shedding dynamic, and reduces the hydrodynamic coefficients fluctuations. There is significant influence of transient pitching motion on the cavitation dynamics. For the fast pitching velocity, a relatively long sheet cavity develops from the leading edge to the midchord of the foil. The cavity has unsteady behavior, which induces a strong impact on the hydrodynamic coefficients. The rebound and subsequent collapse of the sheet/cloud cavity followed by cloud cavitation leads to the significant change of the hydrodynamic magnitudes.

3) For the simulations of cavitating flows, the density modification helps to reduce the turbulent viscosity in the cavitating region, which decreases the turbulent kinetic energy in the cavity, as well as around the cavity closure, especially for the fast pitching hydrofoil. The decrease of turbulent kinetic energy leads to an increase of vorticity near the wall that decreases the pressure in the vortex, which leads to increasing cavitation. The level of vorticity is closely related to the vapor fraction contour and the distri-

bution of turbulent kinetic energy. Overall, the Merkle cavitation model with a turbulent viscosity modification shows a good agreement with the experimental visualizations.

This paper helps to improve the understanding of the cavitation behavior occurring during a forced slow and fast pitching motion. The impact of the density correction term and its influence on the cavitation dynamics, vorticity field, and the dynamic coefficients have been highlighted. The paper shows the benefits of this modifications for RANS methods, but also the strong dependence on the vorticity and the generation of vapor, which can lead to unrealistic cavitating behavior, in particular when interacting with vortex dynamics at high angles of attack. The 2D RANS model in the present study is used as a basis of comparison and as a step towards a future 3D implantation. In addition to large eddy simulation (LES) and direct numerical simulation (DNS), hybrid approaches such as filter-based RANS model [47] and partial averaged Navier-Stokes mthod [48, 49] would be used to better illuminate the physical mechanics of the flow structures around the pitching hydrofoil. Additional research is needed to better understand the influence of the local compressibility and baroclinic torque on the cavitation and wake dynamics, as well as turbulent vorticity fields, particularly for cases with elastic body motions. Such research is important because accurate prediction of the cavity and load fluctuations is critical when analyzing the hydroelastic stability, fatigue, noise, vibration, and erosion characteristics of hydraulic machineries.

This work was supported by the National Natural Science Foundation of China (Grant Nos. 11172040 and 51306020). The authors would like to thank Prof. YinLu Young and Dr. Antoine Ducoin for their helpful comments and support.

1 Arndt R E A. Cavitation in fluid machinery and hydraulic structure. Annu Rev Fluid Mech, 1981, 13: 273–326
2 Luo X W, Ji B, Peng X X, et al. Numerical simulation of cavity shedding from a three-dimensional twisted hydrofoil and induced pressure fluctuation by large-eddy simulation. J Fluids Eng, 2012, 134(4): 041202
3 Ji B, Luo X W, Peng X X, et al. Numerical analysis of cavitation evolution and excited pressure fluctuation around a propeller in non-uniform wake. Int J Multiphase Flow, 2012, 43: 13–21
4 Liu Z, Young Y L. Performance-based design and analysis of flexible composite propulsors. J Fluids Struct, 2011, 27: 1310–1325
5 McCroskey W J. Unsteady airfoils. Ann Rev Fluid Mech, 1982, 14: 285–311
6 Carr L W. Progress in analysis and prediction of dynamic stall. J Aircr, 1988, 25: 6–17
7 Carr L W, McCroskey W J. A review of recent advances in computation and experimental analysis of dynamic stall. International Union of Theoretical and Applied Mechanics on Fluid Dynamics at High Angle of Attack, Tokyo, 1992
8 Ohmi K, Coutanceau M, Loc T P, et al. Vortex formation around an oscillating and translating airfoil at large incidences. J Fluid Mech, 1990, 211: 37–60
9 Oshima Y, Natsume A. Flow field around an oscillating foil. 2nd Int Symp on Flow Visualization, Bochum, 1980
10 Freymuth P. Propulsive vortical signatures of plunging and pitching airfoils, AIAA J, 1988, 26: 881–883
11 Koochesfahani M M. Vortical patterns in the wake of an oscillating airfoil, AIAA J, 1989, 27: 1200–1205
12 Lorber P F, Carta F O. Airfoil dynamic stall at constant pitch rate and high Reynolds number. J Aircr, 1988, 25: 548–556
13 Lee T, Gerontakos P. Investigate of flow over an oscillating airfoil. J Fluid Mech, 2004, 512: 313–341
14 Triantafyllou G S, Triantafyllou M S, Grosenbaugh M A. Optimal thrust development in oscillating foils with application to fish propulsion. J Fluids Struct, 1993, 7: 205–224
15 Jumper E J, Schreck S J, Dimnick R L. Lift-curve characteristics for an airfoil pitching at constant rate. J Aircr, 1987, 24: 680–687
16 Ducoin A, Astolfi J A, Deniset F, et al. Computational and experimental investigation of flow over a transient pitching hydrofoil. Eur J Mech/B Fluids Elsevier, 2009, 28: 728–743
17 Joseph D D. Cavitation in a flowing liquid. Phys Rev E, 1995, 51: 1649–1650
18 Knapp R T, Daily J W, Hammitt F G. Cavitation, New York: McGraw Hill, 1970
19 Callenaere M, Franc J P, Michel J M, et al. The cavitation instability induced by the development of a re-entrant jet. J Fluid Mech, 2001, 444: 223–256
20 Wang G, Senocak I, Shyy W, et al. Dynamics of attached turbulent cavitating flows. Prog Aero Sci, 2001, 37: 551–581
21 Huang B, Wang G. Experimental and numerical investigation of unsteady cavitating flows through a 2D hydrofoil. Sci China Tech Sci, 2011, 54: 1801–1812
22 Stutz B, Legoupil S. X-ray measurements within unsteady cavitations. Exp Fluids, 2003, 35: 130–138
23 Foeth E J. The structure of three-dimensional sheet cavitation. Ph.D. Thesis. Delft: Delft University of Technology, 2008
24 Kunz R F, Boger D A, Stinebring D R, et al. A preconditioned Navier-stokes method for two phase flows with application to cavitation prediction. Comput Fluids, Elsevier, 2000, 29: 849–875
25 Singhal A K, Athavale M M, Li H, et al. Mathematical basis and validation of the full cavitation model. J Fluids Eng, 2002, 124: 617–624
26 Coutier-Delgosha O, Fortes-Patella R, Reboud J L. Evaluation of the turbulence model influence on the numerical simulations of unsteady cavitations. ASME J Fluids Eng, 2003, 125(1): 38–45
27 Senocak I, Shyy W. A pressure-based method for turbulent cavitating flow computations. J Comput Phys, 2002, 176: 363–383
28 Kim S, Brewton S. A multiphase approach to turbulent cavitating flows. Proceedings of 27th Symposium on Naval Hydrodynamics, Seoul, 2008
29 Seo J H, Lele S K. Numerical investigation of cloud cavitation and cavitation noise on a hydrofoil section. Proceedings of 7th Int Symp on Cavitation, Ann Arbor, MI, USA, 2009
30 Kubota A, Kato H, Yamaguchi H, et al. Unsteady structure measurement of cloud cavitation on a foil section using conditional sampling technique. J Fluids Eng, 1989, 111(2): 204–210
31 Huang B, Wang G Y, Zhao Y, et al. Physical and numerical investigation on transient cavitating flows. Sci China Tech Sci, 2013, 56(9): 2207–2218
32 Ji B, Luo X W, Peng X X, et al. Three-dimensional large eddy simulation and vorticity analysis of unsteady cavitating flow around a twisted hydrofoil. J Hydrodyn, 2013, 25(4): 510–519
33 Wu J, Wang G, Shyy W. Time-dependent turbulent cavitating flow computations with interfacial transport and filter based models. Int J Numer MethFluids, 2005, 49: 739–761
34 Wang G, Ostoja-Starzewski M. Large eddy simulation of a sheet/cloud cavitation on a NACA0015 hydrofoil. Appl Math Model, 2007, 31(3): 417–447
35 Shen Y T, Peterson F B. Unsteady cavitation on an oscillating hydrofoil. Proceedings of 12th Symp on Naval Hydrodynamics, Washington D C, 1978
36 Shen Y T, Peterson F B. The influence of hydrofoil oscillation on boundary layer transition and cavitation noise. Proceedings of 13th Symp on Naval Hydrodynamics, Tokyo, 1980
37 Franc J P, Michel J M. Unsteady attached cavitation on an oscillating hydrofoil. J Fluid Mech, 1988, 193: 171–189

38 Hart D P, Brennen C E, Acosta A J. Observations of cavitation on a three-dimensional oscillating hydrofoil. Proc ASME Conf on Cavitation and Multiphase, New York, 1990
39 Kato K, Dan H, Matsudaira Y. Lock-in phenomenon of pitching hydrofoil with cavitation breakdown. Int J Ser B Fluids Therm Eng, 2006, 49: 797–805
40 Uchiyama T. Numerical study on bubbly flow around a hydrofoil in pitching and heaving motions. Proc Institute Mech Eng, 2003, 217: 811–816
41 Ducoin A, Astolfi J A, Sigrist J -F. An experimental analysis of fluid structure interaction of a flexible hydrofoil in various flow regimes including cavitating flow. Eur J Mech B/Fluids, 2012, 36: 63–74
42 Merkle C L, Feng J, Buelow P E O. Computational modeling of sheet cavitations. Proceedings of Third International Symposium on Cavitation, Grenoble, 1998
43 Huang B, Ducoin A, Young Y L. Evaluation of cavitation models for prediction of transient cavitating flows around a pitching hydrofoil. Proceedings of 8th International Symposium on Cavitation, Singapore, 2012
44 Menter F R. Improved two-equation k-ω turbulence models for aerodynamic flows. NASA Tech Memorandu, 1992, 34: 103975
45 Huang B, Young Y L, Wang G, et al. Combined experimental and computational investigation of unsteady structure of sheet/cloud cavitation. J Fluids Eng, 2013, 135: 071301
46 Ji B, Luo X W, Wu Y L, et al. Numerical analysis of unsteady cavitating turbulent flow and shedding horse-shoe vortex structure around a twisted hydrofoil. Int J Multiphase Flow, 2013, 51: 33–43
47 Huang B, Wang G Y. Evaluation of a filter-based model for computations of cavitating flows. Chin Phys Lett, 2011, 28(2): 026401
48 Ji B, Luo X W, Wu Y L. Partially-Averaged Navier-Stokes method with modified k-epsilon model for cavitating flow around a marine propeller in a non-uniform wake. Int J Heat Mass Tran, 2012, 55: 6582–6588
49 Huang B, Wang G Y. Partial averaged Navier-Stokes method for time-dependent turbulent cavitating flows. J Hydrodyn, 2011, 23(1): 26–33